

**Electrospun Nanofiber-supported Carbon Aerogel as a Versatile Platform
toward Asymmetric Supercapacitors**

**Feili Lai,^a Yunpeng Huang,^a Lizeng Zuo,^a Huahao Gu,^a Yue-E Miao,^{b,*} and
Tianxi Liu^{a,b,*}**

*^aState Key Laboratory of Molecular Engineering of Polymers, Department of Macromolecular Science, Fudan University, Shanghai 200433, P. R. China. *E-mail address: txliu@fudan.edu.cn; Tel: +86-21-55664197; Fax: +86-21-65640293.*

*^bState Key Laboratory for Modification of Chemical Fibers and Polymer Materials, College of Materials Science and Engineering, Donghua University, Shanghai 201620, P. R. China. *E-mail address: txliu@dhu.edu.cn or yuee_miao@dhu.edu.cn; Tel: +86-21-67874060; Fax: +86-21-67864063.*

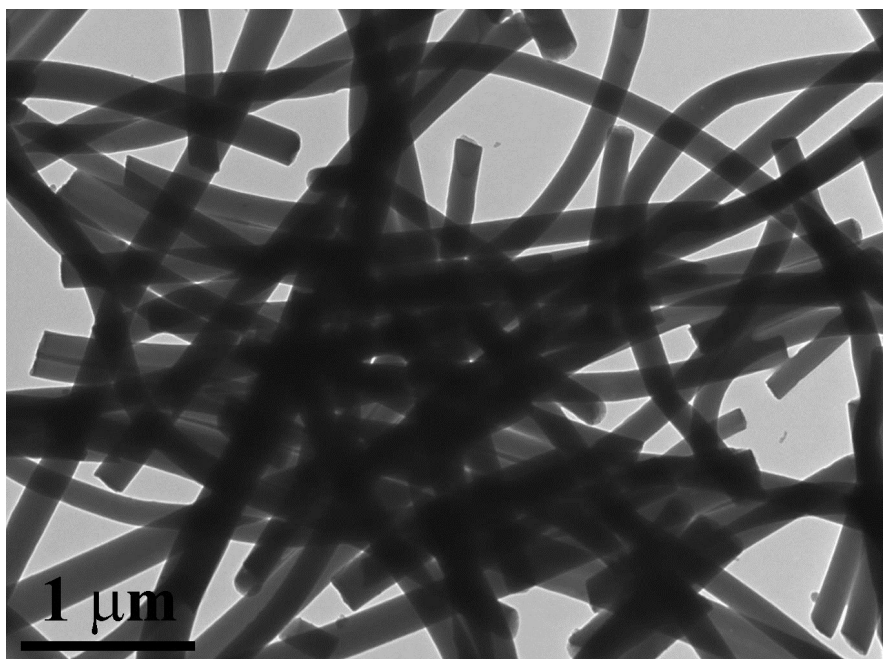


Fig. S1 TEM image of carbon nanofibers derived from o-PAN nanofiber membranes.

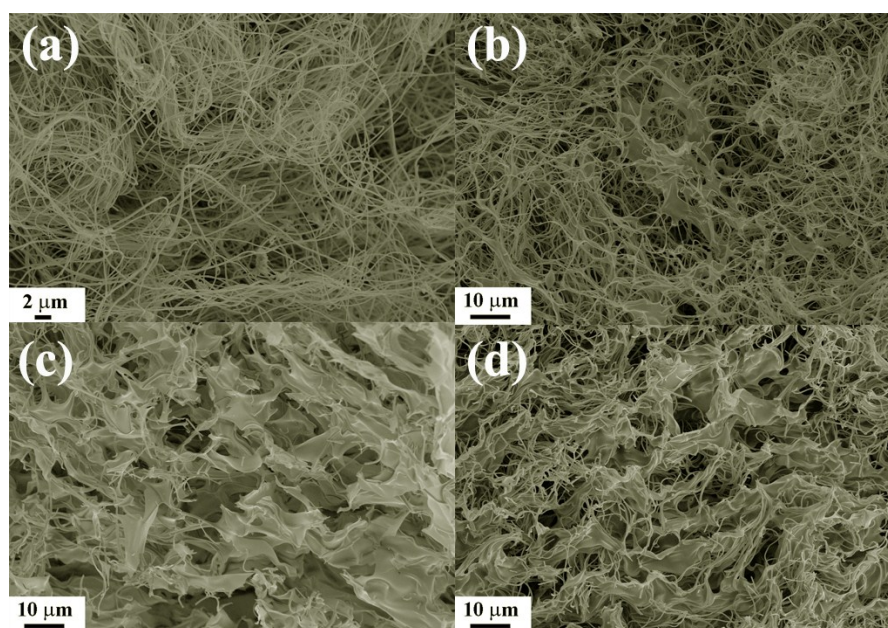


Fig. S2 FESEM images of oPP carbon aerogels with different o-PAN/PAA mass ratios: (a) oPP-0, (b) oPP-16.7, (c) oPP-50, and (d) oPP-33.3 carbon aerogels.

The adsorptive property of oPP-33.3 carbon aerogel.

As shown in Fig. S3a, a series of common pollutants in our daily life as well as from industries are investigated, including commercial oils (*e.g.*, pump oil), fats (*e.g.*, colza oil), water-miscible solvents (*e.g.*, acetone, ethanol), aromatic compounds and their derivatives (*e.g.*, toluene, benzylalcohol). The results show that oPP-33.3 carbon aerogel exhibits a high adsorption capacity toward all of these organic liquids ranging from 20 to 62 times of their original weight, which is attributed to its well-organized and interconnected porous structure for more efficient storage of liquids. More importantly, the adsorption properties of oPP-33.3 carbon aerogel are much higher than those of conventional adsorbents (Table S1), such as graphite oxide foam (10-37 times),¹ carbon nanofiber/carbon foam (~25 times),² conjugated polymers (13-30 times),^{3,4} and so on. The dynamic process for quick adsorption of liquids is also an essential criterion for oPP-33.3 carbon aerogel. As investigated in Fig. S4, oPP-33.3 carbon aerogel can adsorb the liquids rapidly and completely within only several seconds toward chloroform falling down under water. This phenomenon is proposed to be closely related to the enhanced capillary effect from the unique cellular structure consisting of one-dimensional carbon nanofibers and two-dimensional carbon sheets. As shown in Fig. S5, the interconnected carbon nanofibers between carbon sheets will enhance the siphonic effect of the carbon aerogel and act as the driving force for uptake of oils/organic solvents.⁵ Furthermore, recyclability of the adsorbents is also investigated through the combustion process of ethanol (Fig. S6). The results show that the sorption capacity of oPP-33.3 carbon aerogel only drops by 1.3% after five cycles (Fig. S3b). In the case of the recyclable adsorption behavior toward oils/organic solvents with low boiling point (*e.g.*, acetone with the boiling point of 56.5 °C), distillation is applied with the whole process, as displayed in Fig. S7. It can be observed that the adsorption capacity only drops by 3.9% after 5 cycles (Fig. S3c), which further demonstrates the outstanding cycling stability of oPP-33.3 carbon aerogels as versatile adsorbents toward various pollutants.

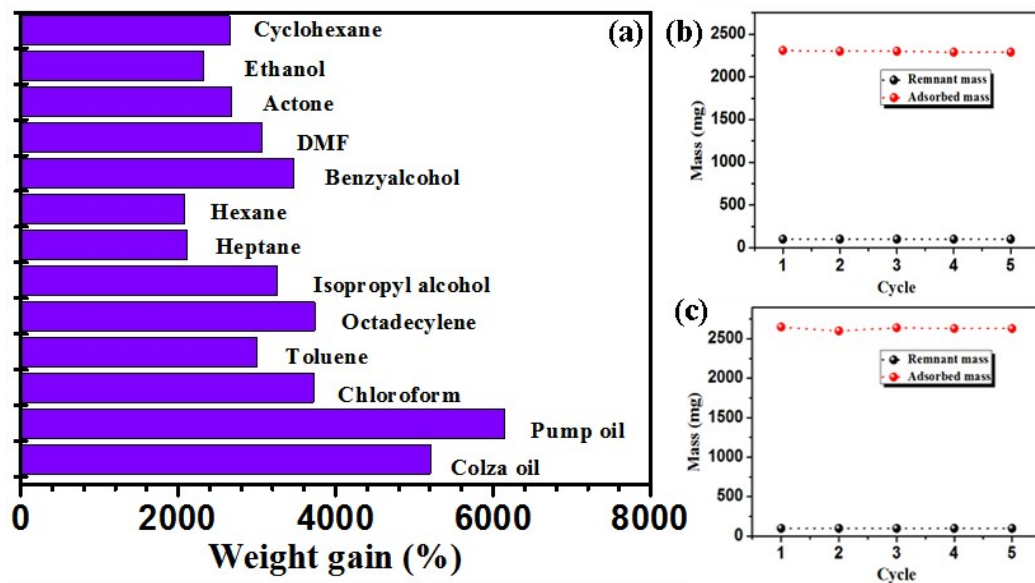


Fig. S3 (a) Adsorption efficiency of oPP-33.3 carbon aerogel toward various organic liquids (Weight gain here is defined as the weight ratio of the adsorbate to the dried oPP-33.3 carbon aerogel). Recycling performance of oPP-33.3 carbon aerogel: (b) The combustion method is used to recycle ethanol; (c) The distillation method is used to recycle acetone.

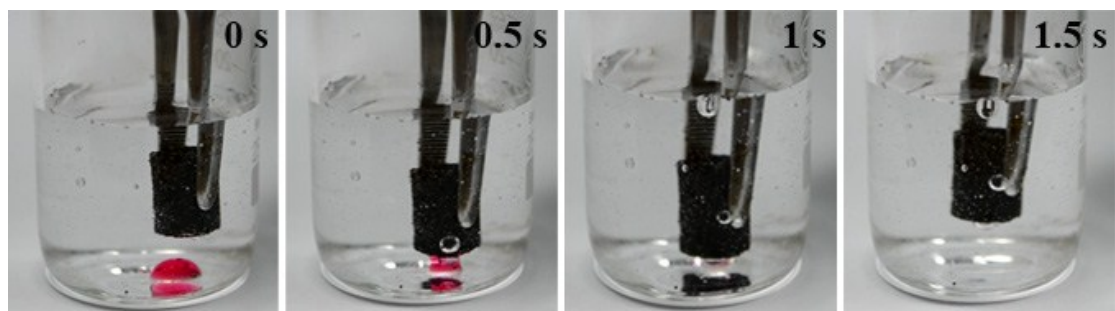


Fig. S4 Photographs showing the adsorption process of chloroform by oPP-33.3 carbon aerogel taken at the time interval of 0.5 s. The red chloroform droplet at the bottom of water is stained with Sudan red 5B.

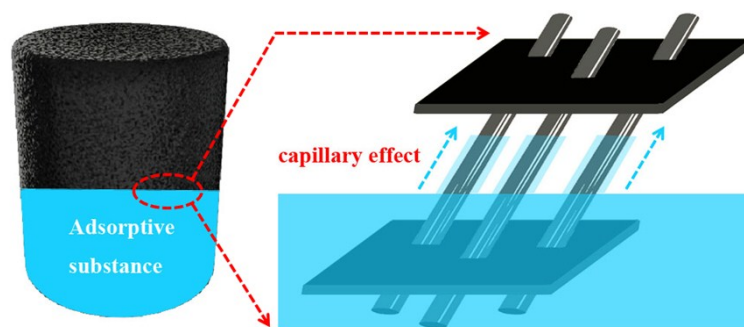


Fig. S5 The illustrated schematic for the probable mechanism of enhanced capillary effect for oPP-33.3 carbon aerogels.



Fig. S6 Photographs showing the generation of oPP-33.3 carbon aerogel via combustion.

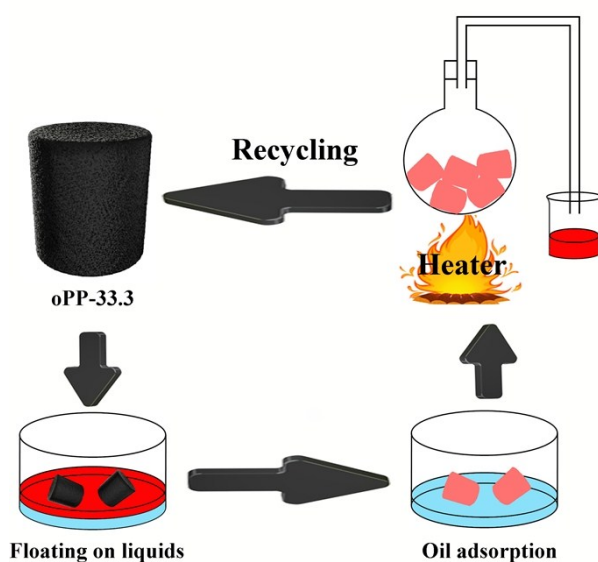


Fig. S7 The recycling process of oPP-33.3 carbon aerogel after its adsorption of acetone.

Table S1. Comparisons of the adsorption capacity of different adsorbent materials.

| Adsorbent materials | Adsorbed substances | Adsorption capacity (g g ⁻¹) | Ref. |
|------------------------------|-----------------------|--|-----------|
| Activated carbon | organic solvents | 0.15-0.64 | 6 |
| Winter melon carbon aerogel | oils/organic solvents | 16-50 | 7 |
| Graphite oxide foam | oils/organic solvents | 10-37 | 1 |
| Superhydrophobic sponges | oils | 13-19 | 8 |
| Conjugated polymers | oils/organic solvents | 13-30 | 3,4 |
| Cellulose aerogel | oils | 34.5 | 9 |
| Carbon nanotube aerogel | oils | 40-80 | 10 |
| Marshmallow-like gels | oils/organic solvents | 6-15 | 11 |
| Carbon nanofiber/carbon foam | oils | 25 | 2 |
| oPP-33.3 carbon aerogels | oils/organic solvents | 20-62 | This work |

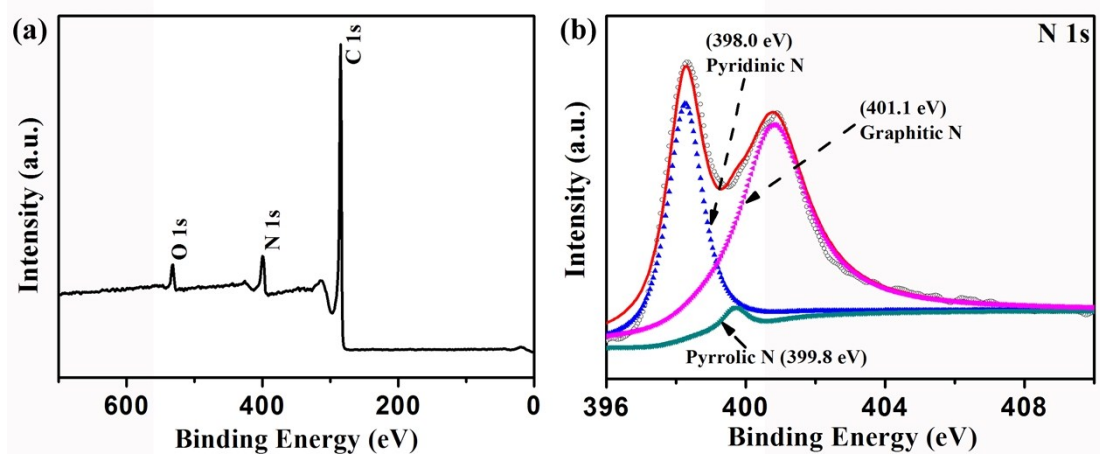


Fig. S8 (a) XPS survey spectrum of oPP-33.3 carbon aerogel; (b) High-resolution N 1s spectrum of oPP-33.3 carbon aerogel.

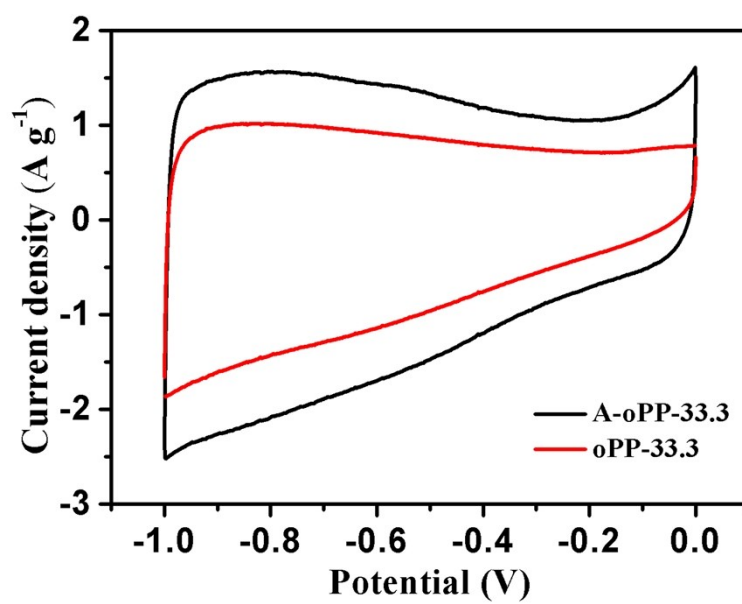


Fig. S9 Comparison of CV curves for A-oPP-33.3 and oPP-33.3 carbon aerogels at a scan rate of 10 mV s⁻¹.

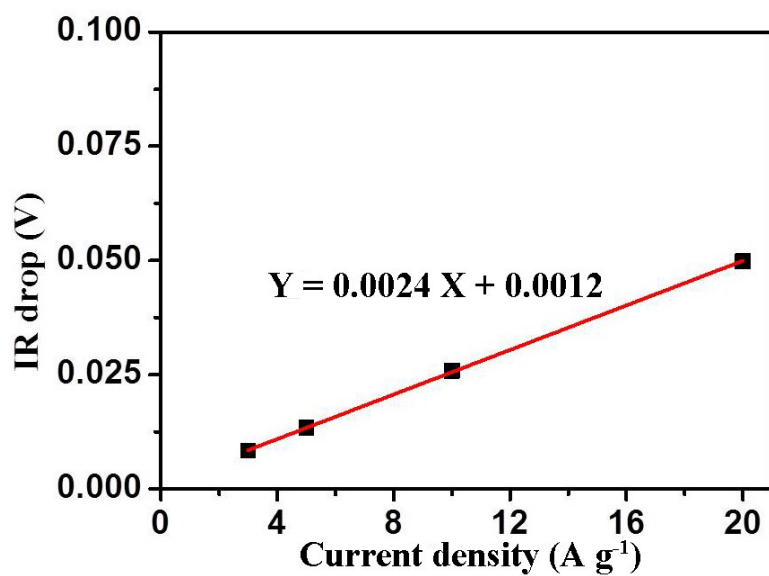


Fig. S10 Internal resistance (IR) drops at different discharge current densities and their corresponding fit lines.

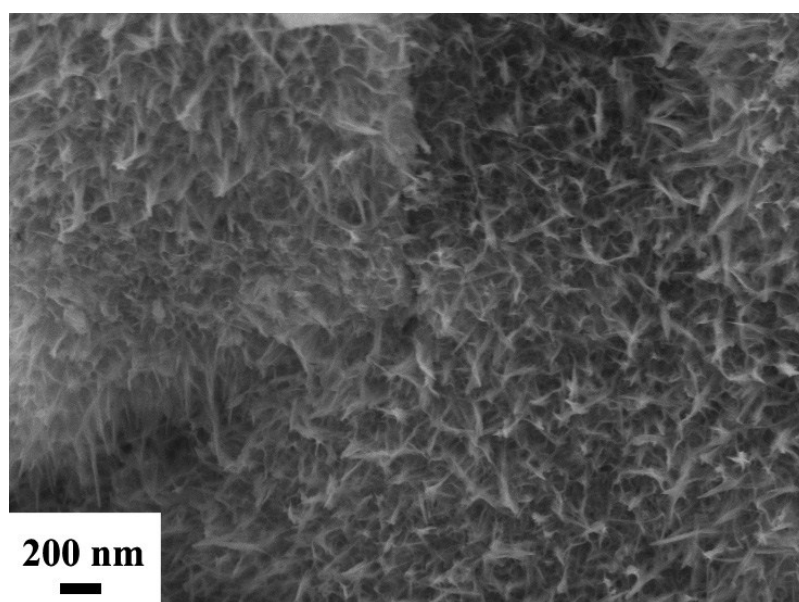


Fig. S11 FESEM image of oPP-33.3@MnO₂-2h hybrid carbon aerogel.

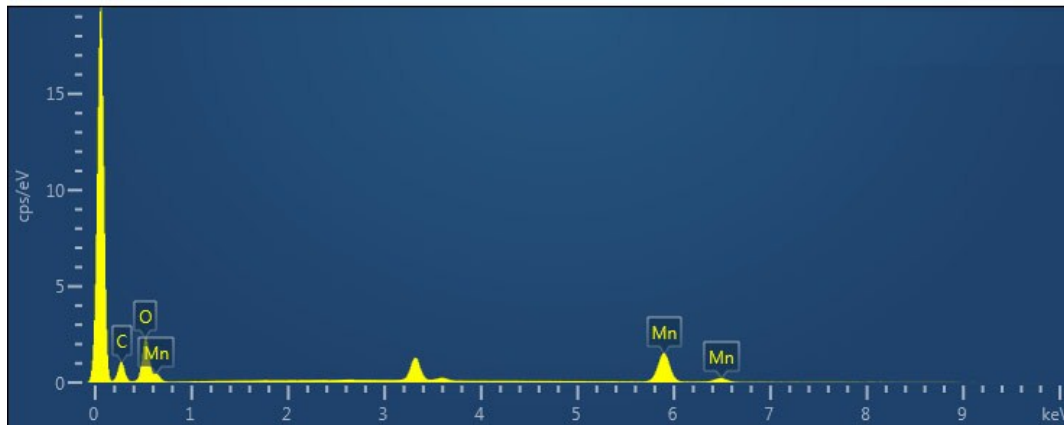


Fig. S12 The corresponding energy-dispersive elemental spectrum of oPP-33.3@MnO₂-2h hybrid carbon aerogel.

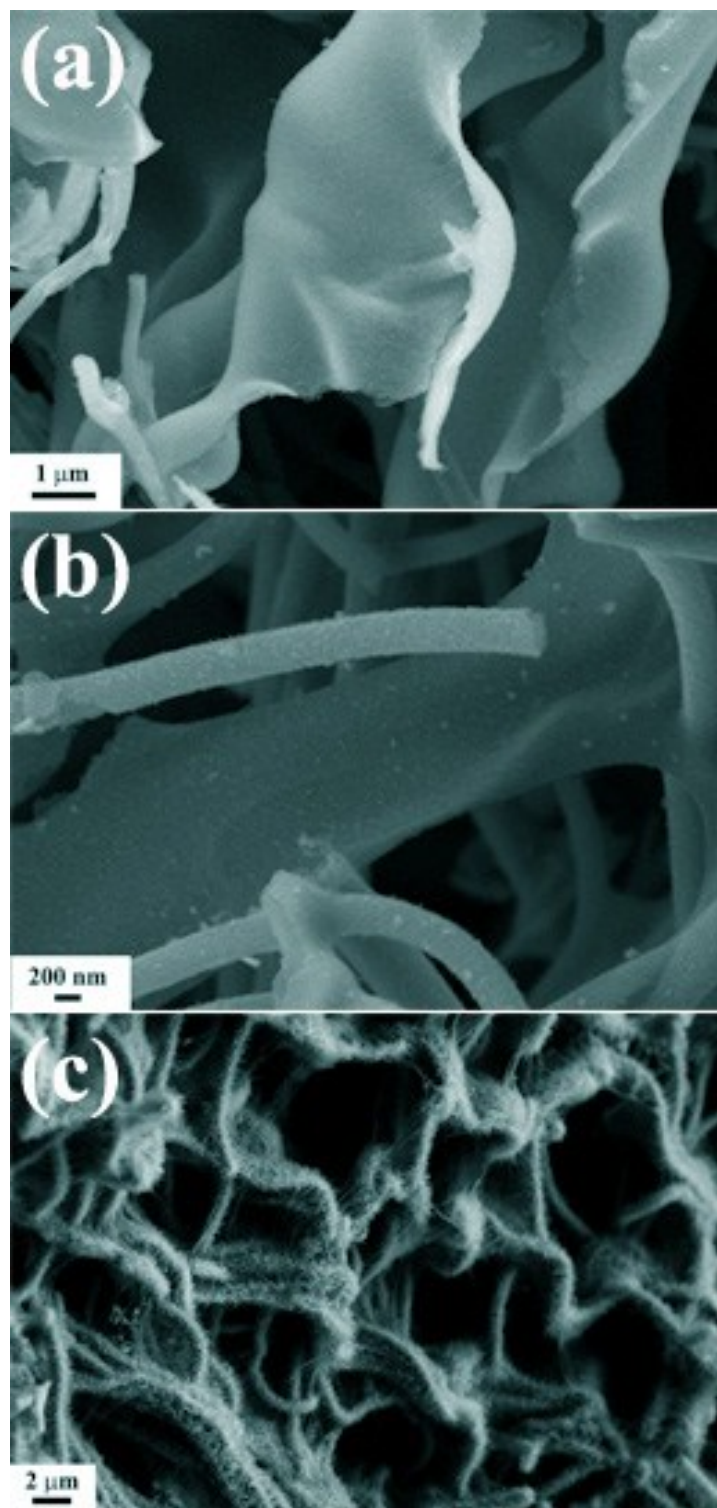


Fig. S13 Typical FESEM images of oPP-33.3@MnO₂-*x*h hybrid carbon aerogels with different deposition time, where: (a) $x = 0.5$, (b) $x = 1$, and (c) $x = 4$.

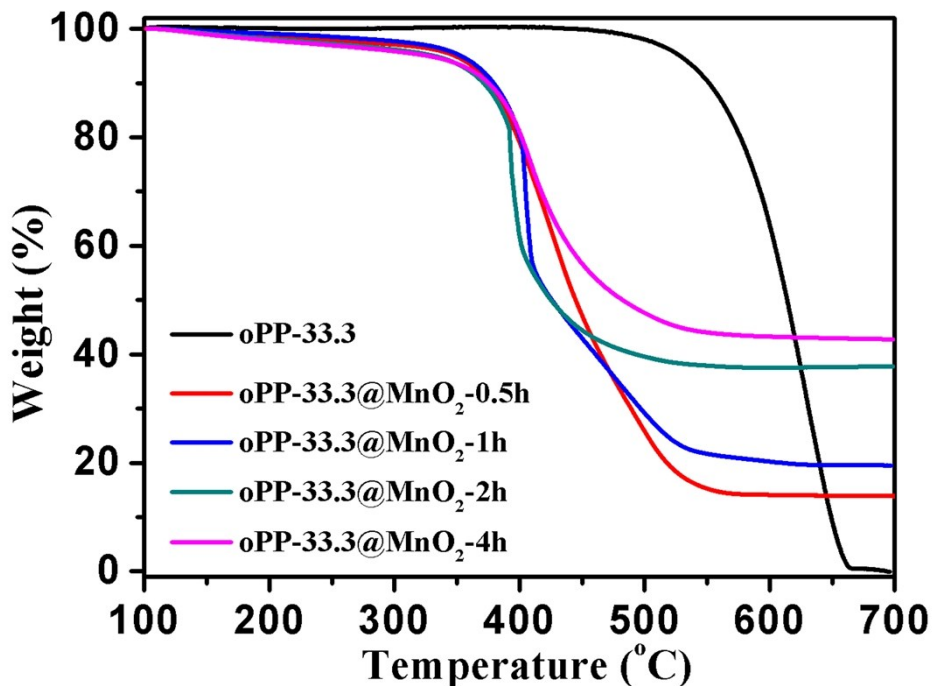


Fig. S14 TGA profiles for oPP-33.3 carbon aerogel, oPP-33.3@MnO₂-0.5h, oPP-33.3@MnO₂-1h, oPP-33.3@MnO₂-2h, and oPP-33.3@MnO₂-4h hybrid carbon aerogels under air flow at a temperature ramp of 20 °C min⁻¹.

Table S2. TGA results of various samples and the corresponding mass ratios of MnO₂ nanosheets.

| Samples | Residual mass (%) | MnO ₂ content |
|---------------------------------|-------------------|--------------------------|
| oPP-33.3 | 1% | -- |
| oPP-33.3@MnO ₂ -0.5h | 13% | ~12% |
| oPP-33.3@MnO ₂ -1h | 20% | ~19% |
| oPP-33.3@MnO ₂ -2h | 38% | ~37% |
| oPP-33.3@MnO ₂ -4h | 43% | ~43% |

The notes for TGA caculation processes of different composites:

Due to the stability of MnO₂ powder before 700 °C, a vital premise that MnO₂ itself keeps 100% retention during TGA test is put forward for further calculation. As shown in Fig. S14, the weight loss of 99% is observed for oPP-33.3 carbon aerogel (black line) from 500 °C to 660 °C, belonging to the cumbustion of carbon materials under air atmosphere.

Hence, the mass loading of MnO₂ nanosheets is denoted as x , and can be caculated from the equation below:

$$x = (y - 0.01) / 0.99$$

where y is the residual weight percentages of various oPP-33.3@MnO₂- x h hybrid carbon aerogels after the TGA tests, respectively.

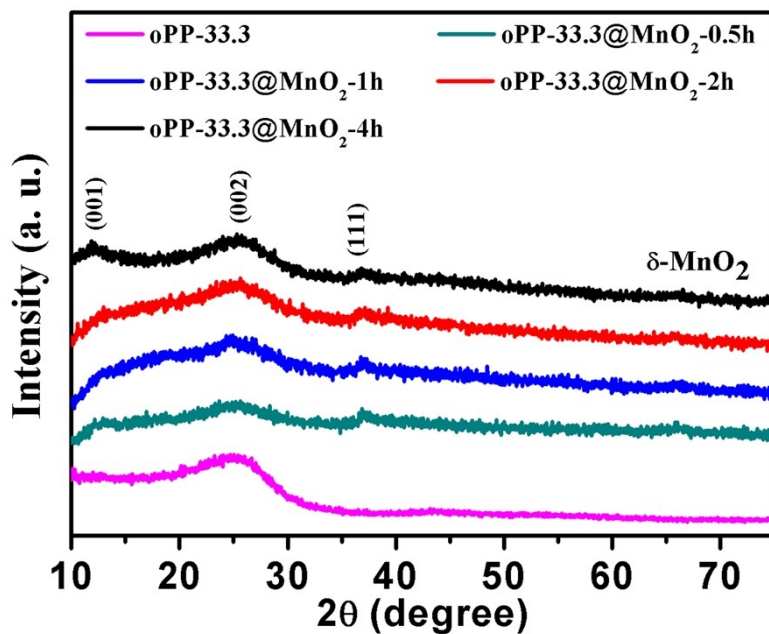


Fig. S15 XRD patterns of oPP-33.3 carbon aerogel, oPP-33.3@MnO₂-0.5h, oPP-33.3@MnO₂-1h, oPP-33.3@MnO₂-2h, and oPP-33.3@MnO₂-4h hybrid carbon aerogels.

Poor crystallinity of oPP-33.3 carbon aerogel can be observed from the pink line in Fig. S15 with a weak peak at $2\theta = 25.4^\circ$. After the redox reaction of KMnO₄ and carbon template, the peak of oPP-33.3 carbon aerogel is covered by the peaks of birnessite-type MnO₂ nanosheets at $2\theta = 12.1^\circ$, 25.8° , and 37.2° . For various oPP-33.3@MnO₂-*x*h hybrid carbon aerogels, the intensity of the peaks is gradually enhanced with the increase of reaction time, which is attributed to the increasing loading amount of MnO₂ nanosheets on oPP-33.3 carbon aerogel.

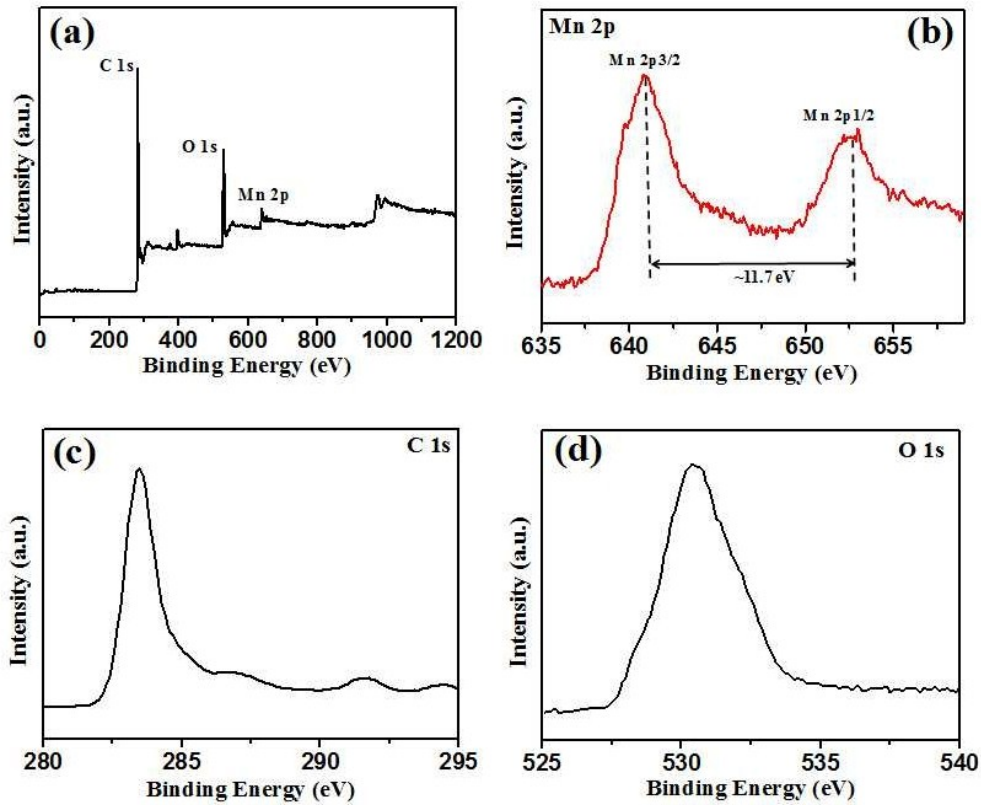


Fig. S16 XPS spectra of the oPP-33.3@MnO₂-2h hybrid carbon aerogels: the full survey scan (a), and high-resolution scans for Mn 2p (b), C1s (c), and O1s (d).

The identification of C 1s, O 1s, Mn 2p peaks from the survey spectra in Fig. S16a indicates the successful fabrication of oPP-33.3@MnO₂ hybrid carbon aerogel. Meanwhile, two peaks at 640.9 eV and 652.6 eV with a spin energy difference of ~11.7 eV are ascribed to Mn 2p_{3/2} and Mn 2p_{1/2} species, respectively (Fig. S16b), indicating the formation of MnO₂ nanosheets.

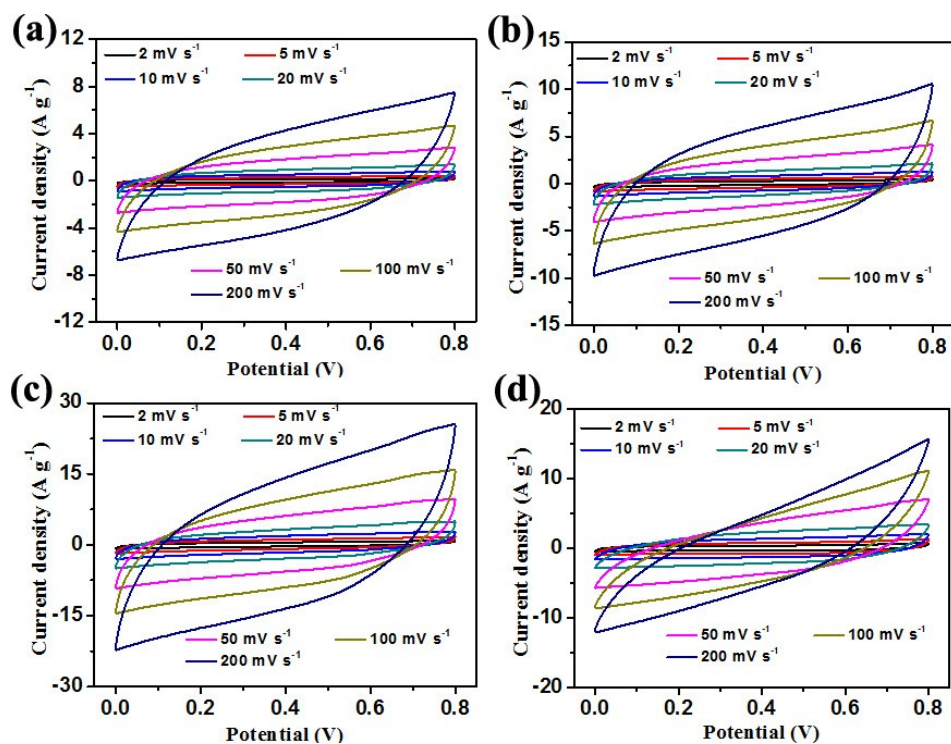


Fig. S17 Cyclic voltammety curves for oPP-33.3@MnO₂-x h hybrid carbon aerogels at various scan rates ranging from 2 mV s⁻¹ to 200 mV s⁻¹: (a) x = 0.5 h; (b) x = 1 h; (c) x = 2 h; (d) x = 4 h.

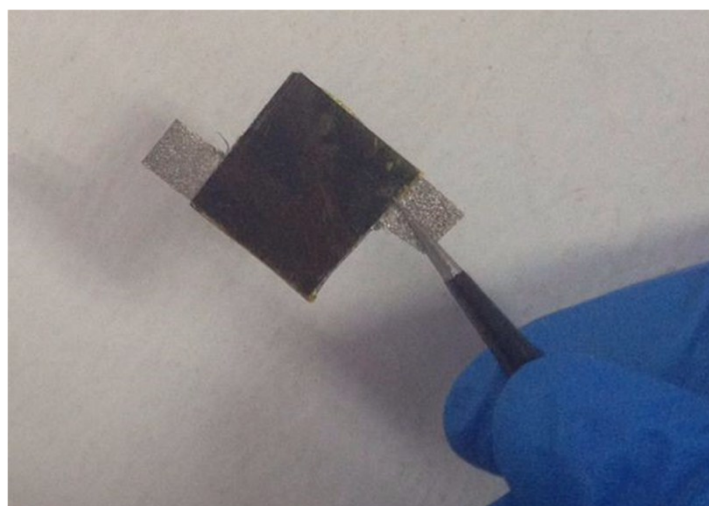


Fig. S18 A digital photograph of the assembled asymmetric supercapacitor oPP-33.3@MnO₂-2h//A-oPP-33.3.

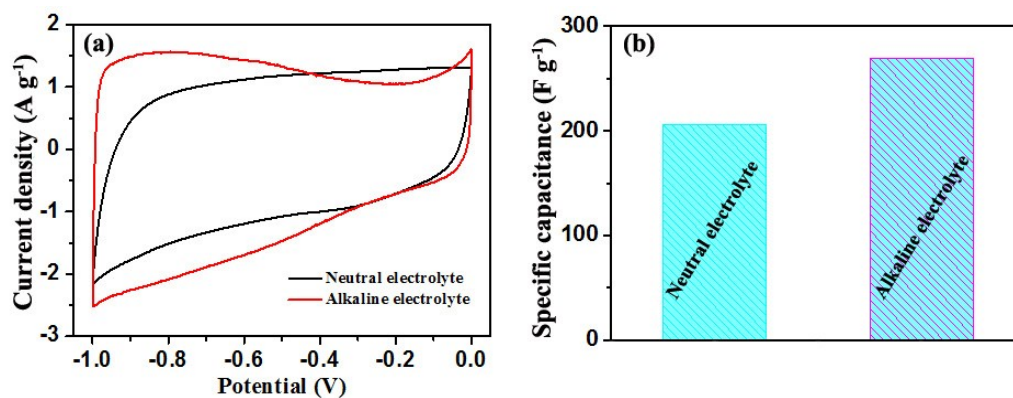


Fig. S19 (a) Cyclic voltammetry in a three-electrode cell system using A-oPP-33.3 carbon aerogel as the working electrode with different electrolyte of 6.0 M KOH and 1.0 M Na₂SO₄ solutions, respectively; (b) The corresponding specific capacitance of A-oPP-33.3 carbon aerogel electrode at a scan rate of 20 mV s⁻¹.

The A-oPP-33.3 carbon aerogel displays excellent electrochemical properties under both neutral and alkaline electrolytes of 1.0 M Na₂SO₄ and 6.0 M KOH solutions. As shown in Fig. S19a, the specific capacitance of A-oPP-33.3 carbon aerogel is 206.4 F g⁻¹ at a scan rate of 10 mV s⁻¹ (Fig. S19b), which is better than previous works on carbon based electrode materials.

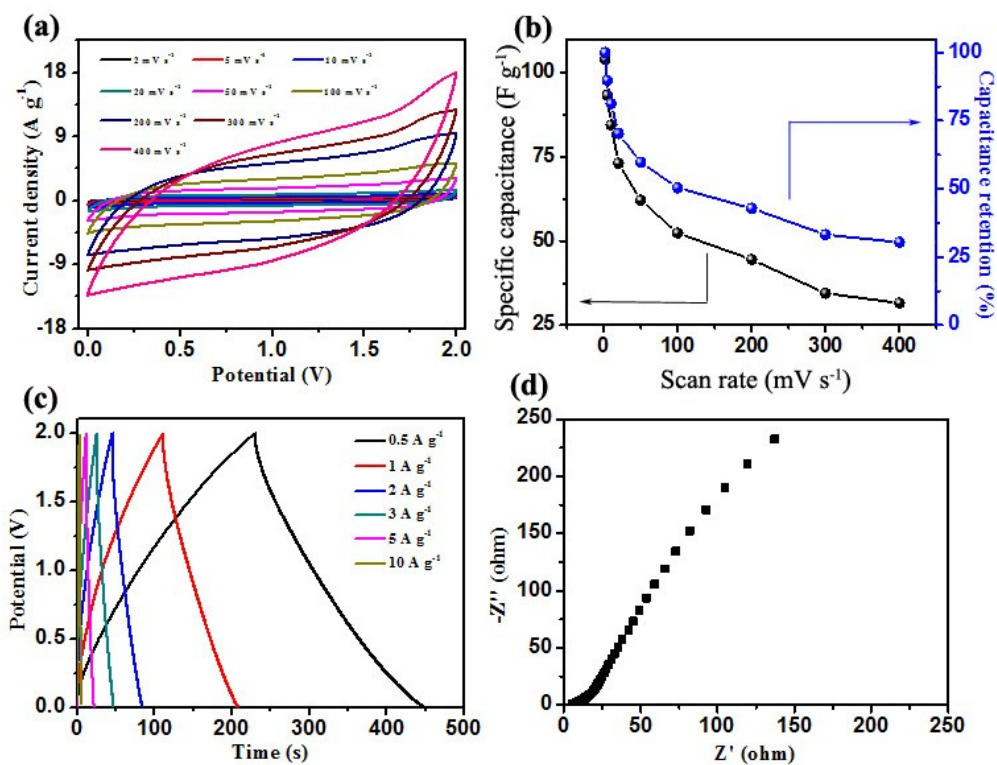


Fig. S20 (a) CV curves of the oPP-33.3@MnO₂-2h//A-oPP-33.3 asymmetric supercapacitor between 0 and 2 V at different scan rates from 2 to 400 mV s⁻¹; (b) Specific capacitance and the corresponding capacitance retention of oPP-33.3@MnO₂//A-oPP-33.3 asymmetric supercapacitor at different scan rates from 2 to 400 mV s⁻¹; (c) Galvanostatic charge/discharge curves of the asymmetric supercapacitor under different current densities; (d) Nyquist plot of oPP-33.3@MnO₂//A-oPP-33.3 asymmetric supercapacitor.

Fig. S20a shows the CV curves of oPP-33.3@MnO₂-2h//A-oPP-33.3 asymmetric supercapacitors between 0 and 2 V at different scan rates from 2 to 400 mV s⁻¹ in 1.0 M Na₂SO₄ electrolyte. Obviously, the CV curves retain good rectangularity even at a high scan rate of 400 mV s⁻¹, indicating its excellent rate stability with small resistance. The specific capacitance of the asymmetric supercapacitor is calculated to be about 103.9 F g⁻¹ at a scan rate of 2 mV s⁻¹ (Fig. S20b), based on the total mass of active materials from both positive and negative electrodes. Even at a high scan rate of 400 mV s⁻¹, the assembled asymmetric supercapacitor (ASC) devices still deliver a high specific capacitance of 31.6 F g⁻¹ (about 30.4% retention of the maximum value), showing its excellent rate stability. Furthermore, the galvanostatic charge/discharge curves with typical triangular shape and linear voltage time relation are obtained in Fig. S20c, directly illustrating the ideal capacitive behavior of oPP-33.3@MnO₂-2h//A-oPP-33.3 asymmetric supercapacitor. In addition, electrochemical impedance spectroscopy (EIS) of the assembled ASC device in the frequency range of 100 kHz to 0.01 Hz presents small resistance (Fig. S20d) as a high-performance energy storage device.

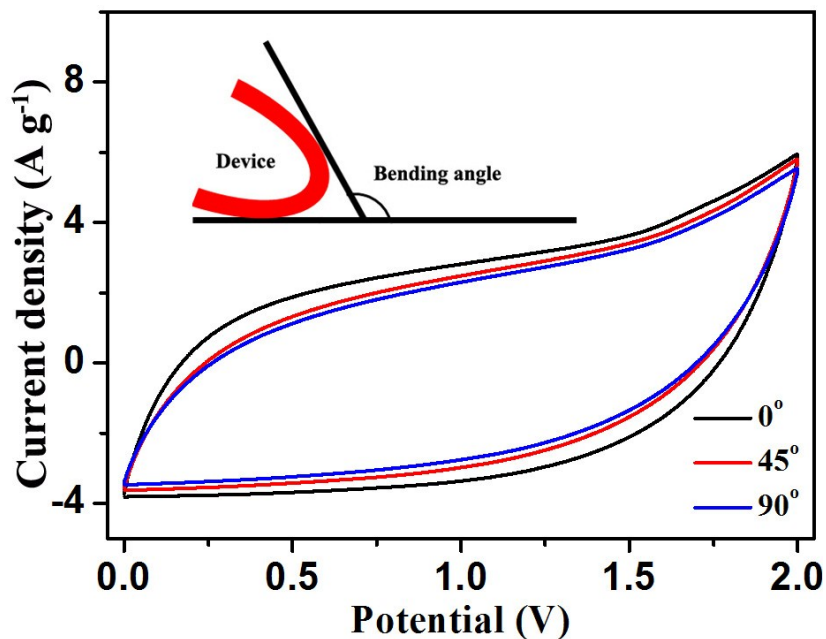


Fig. S21 CV curves of the oPP-33.3@MnO₂-2h//A-oPP-33.3 asymmetric supercapacitor under different bending angles at a scan rate of 50 mV s⁻¹.

The exploration of flexible supercapacitors is a general trend for the development of high-performance and multifunctional energy storage device. As shown in Fig. S21, the CV curves almost display the same shape under different bending angles at a scan rate of 50 mV s⁻¹, indicating negligible capacitive variation for the oPP-33.3@MnO₂-2h//A-oPP-33.3 asymmetric supercapacitors with good flexibility.

References:

- 1 Z. Q. Niu, J. Chen, H. H. Hng, H. Ma and X. D. Chen, *Adv. Mater.*, 2012, **24**, 4144-4150.
- 2 D. Kim, L. J. Zhu, D. J. Jeong, K. Y. Chun, Y. Y. Bang, S. Y. Kim, J. H. Kim and S. K. Oh, *Carbon*, 2013, **63**, 530-536.
- 3 P. X. Si, J. K. Wang, C. Zhao, H. Xu, K. Yang and W. Q. Wang, *Polym. Adv. Technol.*, 2015, **26**, 1091-1096.
- 4 R. X. Yang, T. T. Wang and W. Q. Deng, *Sci. Rep.*, 2015, **5**, 10155-10163.
- 5 X. L. Yao, W. J. Yu, X. Xu, F. Chen and Q. Fu, *Nanoscale*, 2015, **7**, 3959-3964.
- 6 M. A. Lillo-Rodenas, D. Cazorla-Amoros and A. Linares-Solano, *Carbon*, 2005, **43**, 1758-1767.
- 7 Y. Q. Li, Y. A. Samad, K. Polychronopoulou, S. M. Alhassan and K. Liao, *ACS Sustain. Chem. Eng.*, 2014, **2**, 1492-1497.
- 8 Q. Zhu, Q. M. Pan and F. T. Liu, *J. Phys. Chem. C*, 2011, **115**, 17464-17470.
- 9 R. J. Lin, A. Li, T. T. Zheng, L. B. Lu and Y. Cao, *RSC Adv.*, 2015, **5**, 82027-82033.
- 10 Z. Y. Wu, C. Li, H. W. Liang, J. F. Chen and S. H. Yu, *Angew. Chem.Int. Ed.*, 2013, **52**, 2925-2929.
- 11 G. Hayase, K. Kanamori, M. Fukuchi, H. Kaji and K. Nakanishi, *Angew. Chem.Int. Ed.*, 2013, **52**, 1986-1989.NE.Bib